CHAPTER 5

Enhanced photocatalytic performance of NiS/ZnO nanocomposite for the remediation of PNP and RhB dye

5.1 Introduction

A healthy environment is required for the survival of the entire biota, but the hazardous discharge from the industries pose a serious problem for the survival of human beings. Non-biodegradable organic pollutants such as phenolic derivatives, organic dyes, pesticides, antibiotics etc. are the major contributor for the contamination of environment as well as water stream (Sun et al., 2017; Tian et al., 2017). Out of these, phenolic derivatives like p-nitrophenol (PNP) and organic dyes are highly toxic to the living beings because of their carcinogenic and mutagenic behavior (Kuşçu and Sponza, 2009; Sood et al., 2015; Jain et al., 2010). Moreover, nitrophenols and other phenolic derivatives are categorized as high priority pollutants by E.P.A. (Santhy and Selvapathy, 2006; Appusamy et al., 2014). So, in order to remove these pollutants from the environment and water stream many efforts have been made to develop economical, eco-friendly and efficient technologies (Ansari et al., 2016; Mokhtar et al., 2014; L et al., 2015). The photocatalytic processes is the most efficient and economical technique to achieve these rationales (Takata and Domen, 2009; Rajeshwar et al., 2008). In the past few decades, a vast number of photocatalysts have been explored and analyzed for the removal of organic pollutants. For the photocatalysis, ZnO is marked as one of the leading semiconductor materials used in the hydrogen evolution reactions, utilization of carbon dioxide, and mineralization of organic pollutants because of its non-toxic nature, high durability, high stability, and low cost. In recent years, most of the photo-catalysts have been developed under the following four categories; 1) heterojunction photo-catalysts; 2) photo-catalysts with multistage structures; 3) nobel metal/semiconductor photo-catalysts; 4) nanomaterials with high electron-mobility material as co-catalysts (Yang et al., 2020). Taking these into consideration, we designed NiS/ZnO hetero-structure photocatalysts for the

mineralization of organic pollutants (PNP and rhodamine B) at the expense of UV-light irradiation. Recent reports demonstrate that the scope of the individual semiconductors as photocatalysts are narrower; since, they do not allow the efficient removal of pollutants because of their larger bandgap and poor capacity of charge separation (Wang et al., 2013; Saravanan et al., 2015; Lee et al., 2015). So, in order to improve the photocatalytic performance, semiconductors are modified by certain dopants or metal oxides. In this regard, various modifications have been done in ZnO semiconductors (H. Zhao et al., 2015; Liu et al., 2019; Liu and Li, 2021; Mirzaei et al., 2018; Zhang et al., 2020; Štrbac et al., 2018; Al Abri et al., 2019; Tobajas et al., 2017) and NiS semiconductor (Nguyen et al., 2018; Xu et al., 2018; Luo et al., 2020; Qian et al., 2018; Wu et al., 2016; He and Guo, 2017; Torki and Faghihian, 2018, 2017) by incorporating suitable guest into hosts to make photocatalysis feasible with a higher quantum efficiency of photocatalyst. The NiS based heterosturctures have been mainly explored and applied for water splitting, electrocatalysis, CO_2 utilization and water remediation. The motivation to use NiS nanoparticles is because of its photochemical properties; it is used as a cocatalyt to enhance the photocatalytic activity by creating an internal electric field at the interface of the nanocomposites which helps in the efficient charge separation between photogenerated excitons (e^-/h^+) and creates large number of reaction sites for photocatalysis (Luo et al., 2020; Wu et al., 2016; Torki and Faghihian, 2018). Therefore, we expect that the nanocomposite NiS/ZnO would be an excellent photocatalyst for the efficient removal of non-biodegradable PNP and RhB dye from water with a restrained charge recombination rate and strong redox ability. To best of our knowledge there is only one article on NiS/ZnO that was published by Perfecto et al. in 2021; in this article authors applied the nanocomposite for the sensing of butanone analyte.

However, NiS/ZnO heterostructure was not explored for water remediation process till date. We first time report its photocatalytic property mainly for the removal of the PNP and RhB dye from aqueous medium.

5.2 Experimental

5.2.1 Synthesis of ZnO

Typically, 0.04 M aqueous solution of sodium citrate tribasic dihydrate was mixed with 0.02 M alcoholic solution of zinc nitrate hexahydrate under continuous stirring. The mixed solution was transferred into Teflon lined stainless steel autoclave, tightly sealed, and it was kept in a hot air oven for 16 h at 200 °C. After completion of the reaction the autoclave was allowed to cool at room temperature and the sample solution was centrifuged. Later the solid material obtained was washed 4–5 times with double distilled water and ethanol and then the sample was collected and dried at 70 °C. The resulting white powder was calcined at 500 °C for 2 h in a muffle furnace to obtained ZnO (A-1) nanoparticle (figure 5.1a).

5.2.2 Synthesis of NiS

For synthesizing NiS (B-1) all the conditions are the same as used for the synthesis of ZnO nanoparticles except $Zn(NO_3)_2.6H_2O$ replaced by $Ni(NO_3)_2.6H_2O$ and thiourea (0.08 M) was additionally added in the mixed solution (figure 5.1b).

5.2.3 Synthesis of NiS/ZnO

0.1 M ZnO and xM NiS (x = 0.012, 0.014, 0.016) as obtained from above was dispersed in 50 mL water by ultrasonication for 2 h. The resulting suspended sample solution was centrifuged and washed with double distilled water and ethanol; further the sample was dried in an oven at 70 °C; the obtained powder is NiS/ZnO nanocomposites (figure 5.1c). For the sake of simplicity different samples of NiS (0.012, 0.014 and 0.016 M) loaded with ZnO

nanocomposites are named as AB-1, AB-2 and AB-3 respectively for rest of the study.

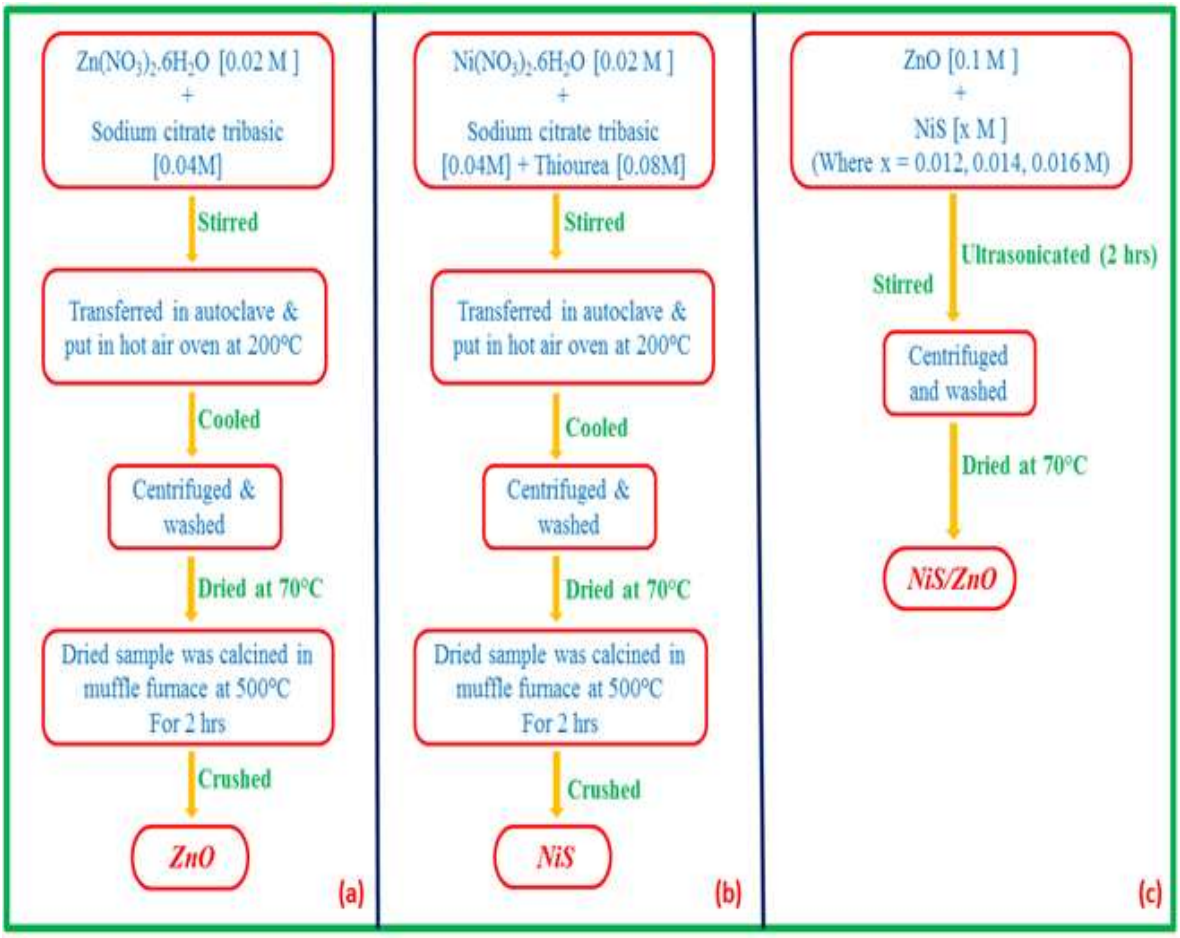

Fig. 5.1 Schematic diagram for the synthesis of (a) ZnO (b) NiS, and (c) NiS/ZnO nanocomposites

5.3 Characterization details

Above prepared photocatalysts were characterized by different techniques discussed in chapter 2.

5.3.1 Measurement of photocatalytic activity

The photocatalytic efficiency of the synthesized catalysts was evaluated by photo-assisted catalytic degradation of PNP and RhB dye as a model pollutant. The photocatalytic experiment was carried out by using UV-light (Phillips, 8 W, 254 nm) as an irradiation

source. Certain known amount (0.12 g/L) of the photo-catalysts was added separately to the fixed concentration (1.01×10^{-4} mol/L PNP and 2.01×10^{-5} mol/L of RhB) of the pollutant, moreover the suspension was allowed to stir in dark to achieve adsorption-desorption equilibrium. After that sample solution was irradiated with UV light source and at regular time interval UV-Vis absorption spectrum of the suspension was recorded by UV-Vis spectrophotometer. The continuous decrease in the absorption intensity of model pollutant (PNP and RhB) determines the degradation efficiency of the photocatalysts. The degradation percentage of PNP and RhB was calculated by using equation (3.1).

To determine the active species generated during the process of photocatalysis, equal concentrations of the p-benzoquinone (PBQ), iso-propyl alcohol (IPA), and potassium iodide (KI) scavengers are used separately to trap superoxide radical ($O_2^{\bullet -}$), hydroxyl radical ($OH^{\bullet}$) and holes (h^+) respectively.

5.4 Results and discussion

5.4.1 HR-XRD

The crystallinity and the phase structure of the synthesized samples were investigated by high resolution X-ray diffraction (HR-XRD) pattern. Figure 5.2a shows HR-XRD patterns of ZnO, NiS and NiS/ZnO nanocomposites with different molar ratio of NiS samples. The diffraction patterns corresponding to A-1 is observed at 2θ values 31.85°, 34.40°, 36.21°, 47.50°, 56.61°, 62.91°, 66.47°, 68.01°, 69.11° which are indexed at (100), (002), (101), (102), (110), (103), (200), (112), and (201) planes of cubic crystal structurere. The characteristic diffraction peaks for NiS was observed at 2θ values 30.15°, 34.57°, 45.75°, 53.42°, 60.72°, 62.50°, 65.11°, 70.61°, and 72.85°; corresponding to (100), (101), (102), (110), (103), (200), (201), (004), and (202) planes of the hexagonal crystal structure. The

diffraction peaks of A-1 and B-1 are in good agreement with the standard database (JCPDS no. 01–1136 and 02–1280 respectively) which, confirms that synthesized materials are pure and crystalline in nature. Moreover, the different NiS/ZnO nanocomposites display the common peaks of both ZnO and NiS, which is very similar to the diffraction peaks of the Srinivasa Rao et al. (Rao, 2020).

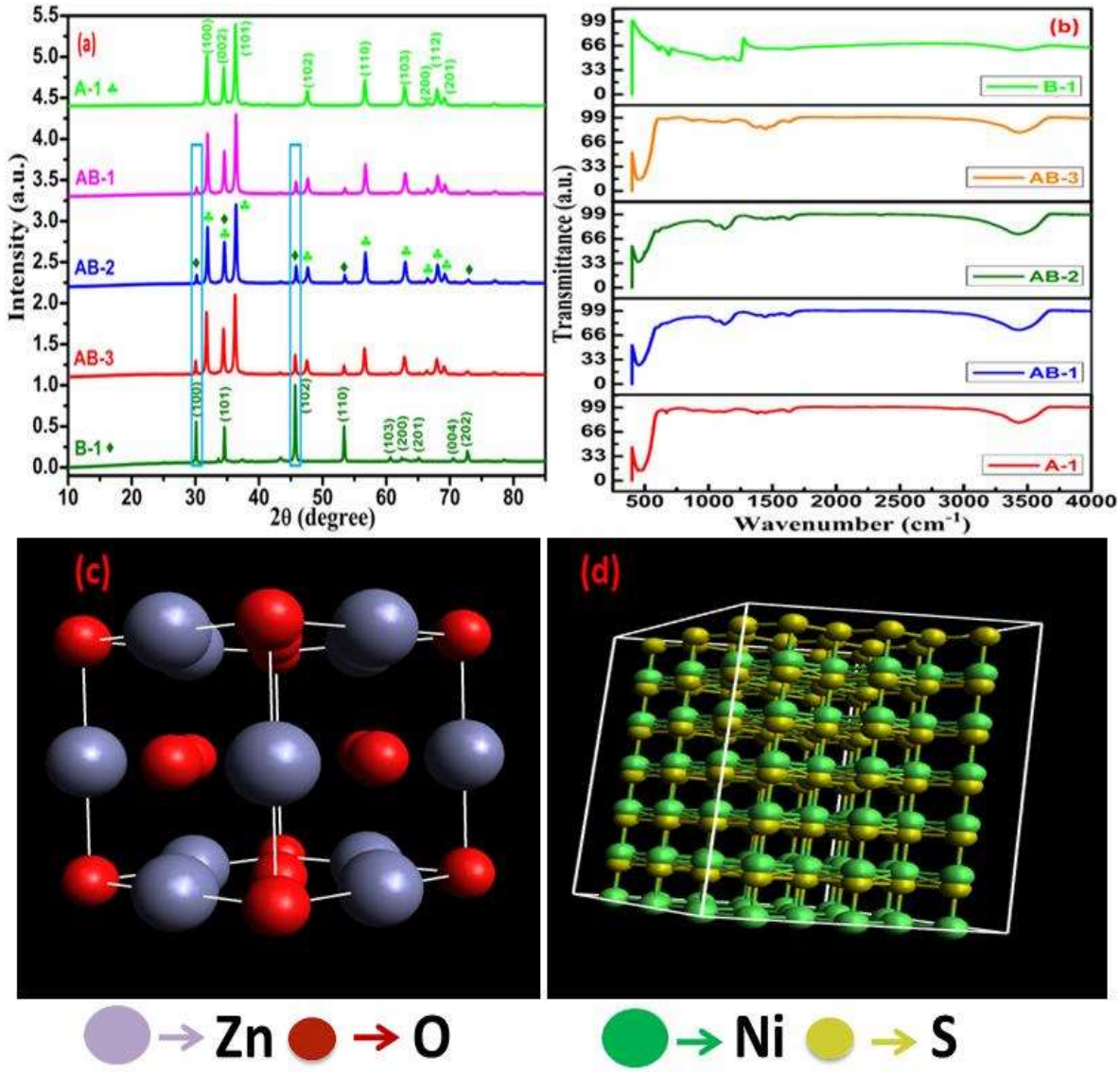

Fig. 5.2 (a) HR-XRD pattern of A-1, B-1, AB-1, AB-2, & AB-3 samples (b) FT-IR of A-1, AB-1, AB-2, AB-3, and B-1 samples, (c, d) Crystal structures of A-1 and B-1 respectively

The intensity of the NiS peaks increases to some extent with increasing the amount of NiS (peaks in the boxes). Besides above characteristics peaks there are no other extra peaks observed which confirms the purity of the samples. Furthermore, the crystallite sizes of the prepared samples were calculated by using the well known Debye-Scherrer equation (Langford and Wilson, 1978; Klug and Alexander, 1974).

$$D = \frac{k\lambda}{\beta \cos\theta} \qquad (5.1)$$

Here, k (0.9) denotes the shape coefficient of the crystal and λ (0.15406 nm) is the wavelength of X-ray while, β represents the full width at half-maximum (FWHM) of the diffraction peak (β in radian) and θ denotes the Bragg angle. The calculated average crystallite sizes of A-1, AB-2 and B-1 samples are 28.62, 30.17 and 27.35 nm respectively. As, AB-2 have larger crystallite size than A-1 and B-1; we know that generally the larger crystallite size also responsible for the enhancement of photocatalytic activity (Nandiyanto et al., 2020; Sharma et al., n.d.). Figure 5.2 c and d displays the crystal structures of ZnO (A-1) and NiS (B-1) respectively.

5.4.2 FT-IR

For knowing the type of vibrations present in the sample we recorded the FT-IR spectrum of the samples, the results of which is shown in the figure 5.2b. The broad absorption band obtained around 3350-3440 cm^{-1} and 1350-1550 are corresponding to the stretching and bending vibration in O–H bond of H_2O respectively, which, adsorbs from the unavoidable atmospheric moisture while, the absorption peaks appeared around 435-500 cm^{-1} is due to stretching in Zn-O bond (Nagaraju et al., 2017; Buazar et al., 2016; Nagarajan and Arumugam Kuppusamy, 2013). The absorption band at around 670 cm^{-1} in B-1 is due to vibrational stretching present in Ni-S bond (Jansi Rani et al., 2019). In the recorded spectrum

we found weak bands for all samples, which confirm that the adsorption is physical and in the recorded spectrum we can't obtain any other vibrational peaks means synthesized samples, are free from impurity.

5.4.3 Morphological analysis (TEM and FE-SEM)

TEM micrographs are the representative of the morphological behavior of the synthesized nanoparticles. Figure 5.3a represents the TEM image of AB-2 nanocomposite which is almost spherical shape and highly crystalline in nature. HR-TEM of AB-2 is shown in figure 5.3b depicts a close interfacial contact between ZnO and NiS nanoparticles which are confirmed by the d-spacing value of the corresponding lattice fringes. The calculated d-spacing for ZnO and NiS was found to be 0.15 nm and 0.48 nm respectively, which are corresponding to the [110] plane for both. Figure 5.3c displays the elemental mapping of the AB-2 which validates that all the elements (Zn, O, Ni and S) are present in the nanocomposite. The average particle size of AB-2 nanocomposite was calculated as 34 nm (figure 5.3d). The TEM image of A-1 nanoparticle is given in figure 5.3e; the figure shows that the particles are spherical in shape and the SAED pattern confirms the polycrystalline nature of A-1 sample (inset of figure 5.3e). However, B-1 attains the cylindrical (figure 5.3f) morphology and the formation of single crystal phase (inset of figure 5.3f) takes place. Thus, the observed results like crystallinity and crystallite size of the HR-TEM and SAED were found very close to the HR-XRD results.

With help of FE-SEM techniques the surface morphology and distribution of the nanoparticles were visualized. Figure 5.4 depicts the morphology of A-1, B-1 and AB-2 nanoparticles. Figure 5.4a displays the FE-SEM micrograph of A-1 nanoparticles which is of spherical shape while, FE-SEM micrograph of B-1 sample shows that it attains the flower

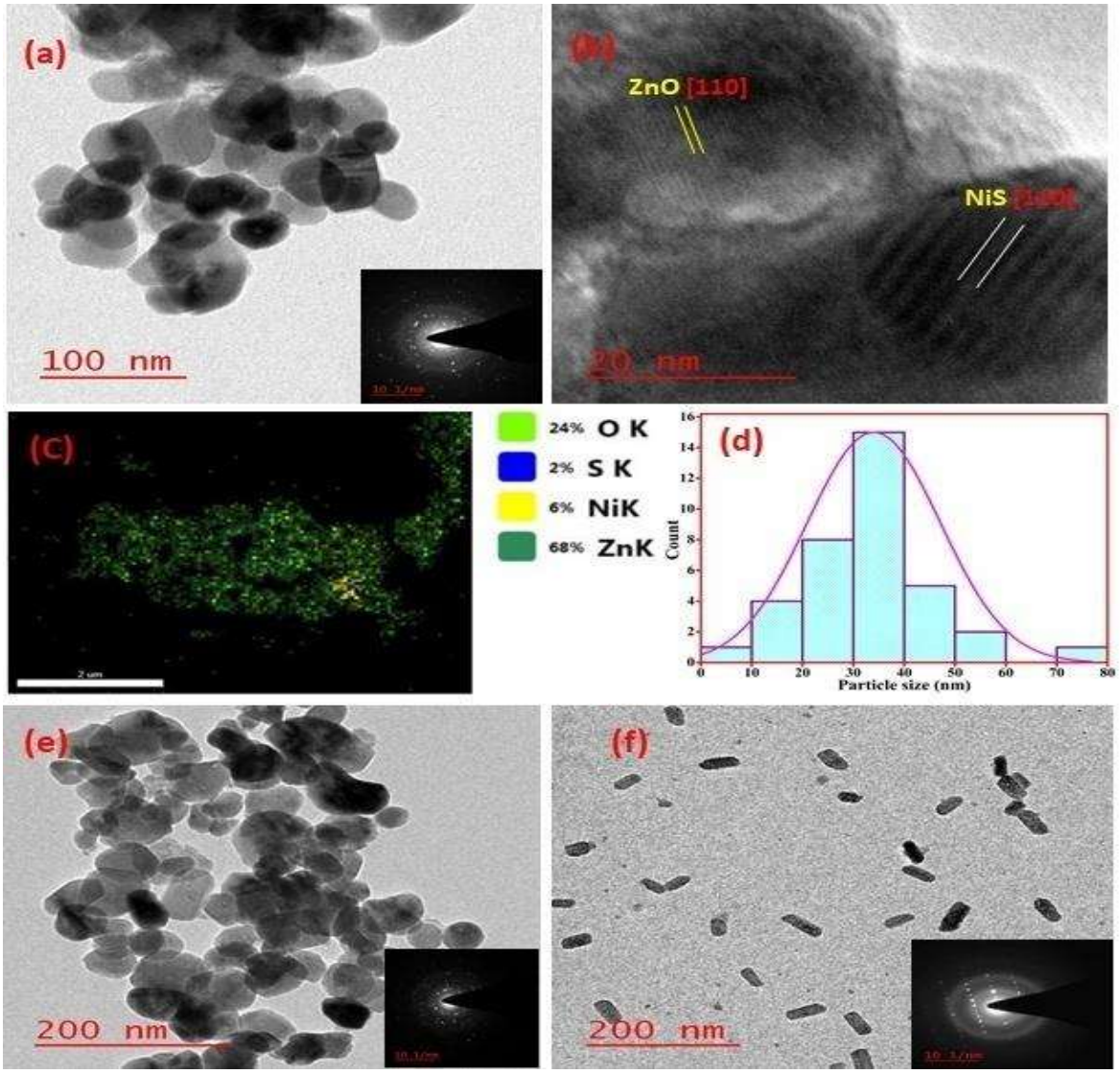

Fig. 5.3 (a) TEM micrograph of AB-2 (inset showing SAED), (b) HR-TEM of AB-2, (c) Elemental mapping of AB-2, (d) Histogram of average particle size of AB-2, (e) TEM image of B-1, and (f) TEM image of A-1

Like morphology (figure 5.4b). The FE-SEM image of AB-2 nanocomposite displayed in figure 5.4c which depict that nanocomposite has beads like structure containing tiny pores on the surface with uniform distribution of NiS over the ZnO surface. The sample AB-2 was also characterized by EDS measurement for further confirmation of the elemental distribution in the synthesized heterostructure (figure 5.4d) which confirms the presence of

basic constituents of the heterostructure i.e., Zn, O, Ni and S. Interplaner assembly of NiS with ZnO nanoparticles was proved by the distinct elemental signals observed in the EDS measurement.

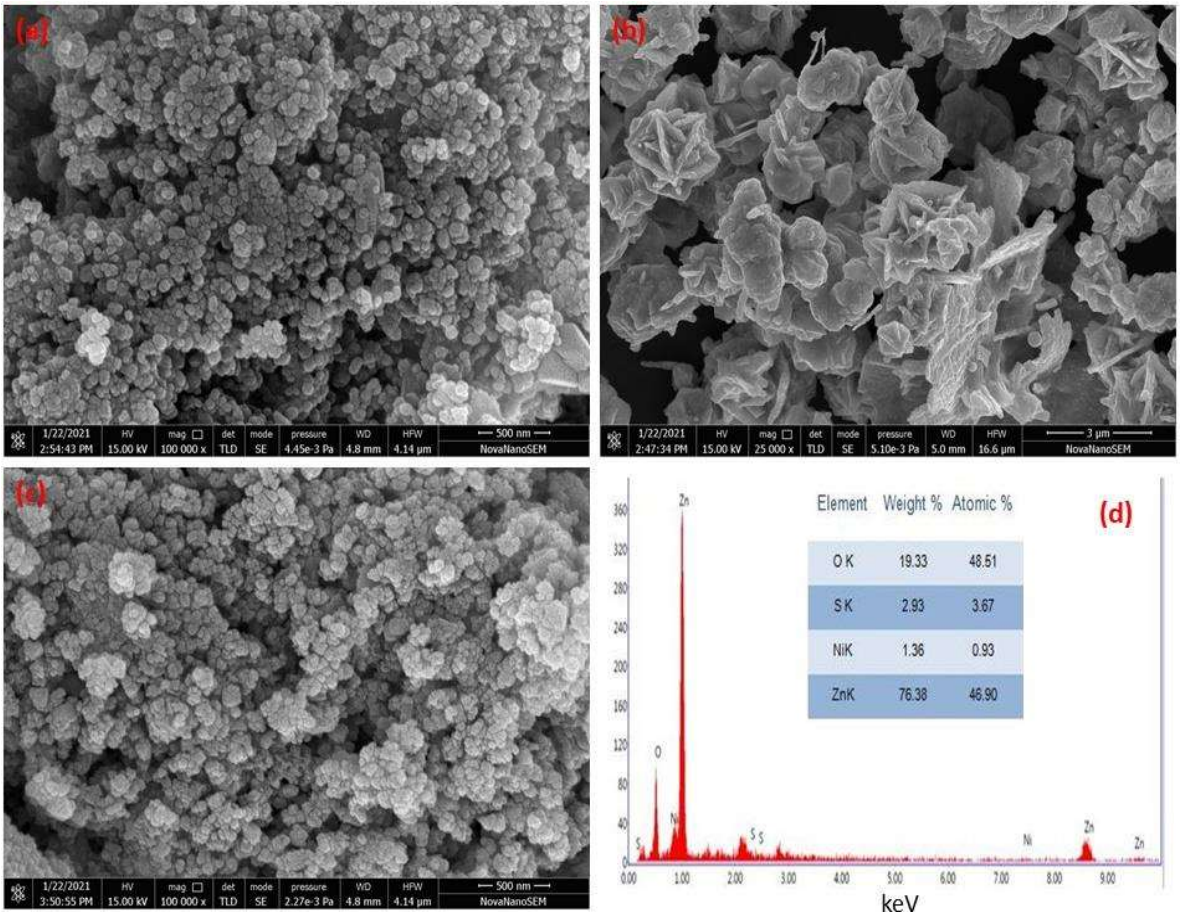

Fig. 5.4 FE-SEM images of (a) A-1, (b) B-1, (c) AB-2, and (d) EDS of AB-2

5.4.4 XPS analysis

To develop deep understanding about the chemical states and types of binding involved in the nanocomposite the AB-2 sample was characterized through XPS spectroscopy. The results of XPS analysis is given in figure 5.5; figure 5.5a, shows two symmetrical peaks at 1021.32 eV and 1044.80 eV corresponding to Zn $2P_{3/2}$ and Zn $2P_{1/2}$ respectively. Figure 5.5b displays XPS spectra of oxygen at 530.47 eV and 531.62 eV. The peak at 530.47 eV is due to

the absorption of oxygen atom on the surface of ZnO while the second peak at 531.62 eV is because of presence of oxygen in the crystalline structure. XPS spectra of Ni gave peaks at 855.31, 861.38, 873.01, and 880.14 eV (figure 5.5c) out of which peaks at 855.31 and 873.01 eV corresponds to the Ni^{+2} $2P_{3/2}$ and Ni^{+2} $2P_{1/2}$ microstate and remaining two peaks at 861.38 & 880.14 eV are the satellite peaks of the Ni^{+2} state.

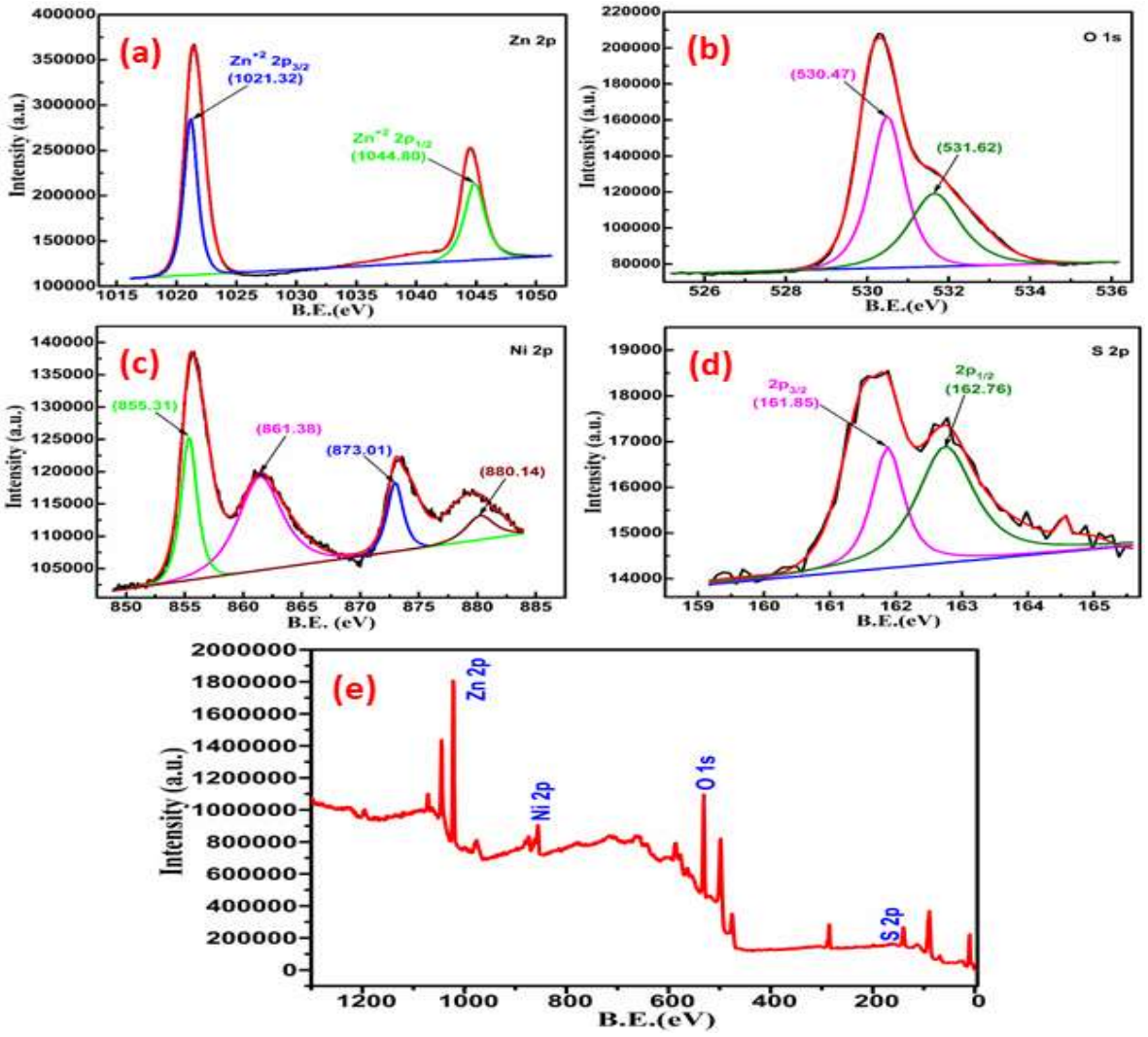

Fig. 5.5 XPS spectrum of (a) Zn (2p), (b) O (1s), (c) Ni (2p), (d) S (2p) and (e) XPS survey spectrum of AB-2. (Note: labeled peaks in figure a-c were obtained from XPS PEAK 41 software)

As displayed in figure 5.5d; sulfur gives two characteristic peaks at 161.85 and 162.76 eV corresponding to $2P_{3/2}$ and $2P_{1/2}$ state of S respectively (Perfecto et al., 2021). XPS survey spectrum of the sample is given in the figure 5.5e which, confirm the presence of the above discussed (Zn, O, Ni and S) element with suitable binding energy.

5.4.5 B.E.T. analysis

Specific surface area and mesoporosity of the catalyst play an important role in photocatalysis because a catalyst having larger surface area may produce more active sites (Prasannalakshmi et al., 2016). To investigate the specific surface area and mesoporosity of the sample A-1 and AB-2 we characterized the sample through N_2 adsorption-desorption and BET measurement technique. Figure 5.6a and b displays the results of N_2 adsorption-desorption isotherm for A-1 and AB-2 samples respectively which shows a H3 hysteresis loop with a type IV pattern which supports the mesoporous nature of the sample (Hussein et al., 2013). The specific surface area of the sample A-1 and AB-2 was calculated by using BET equation and it was found to be 2.46 and 8.65 m^2/g respectively.

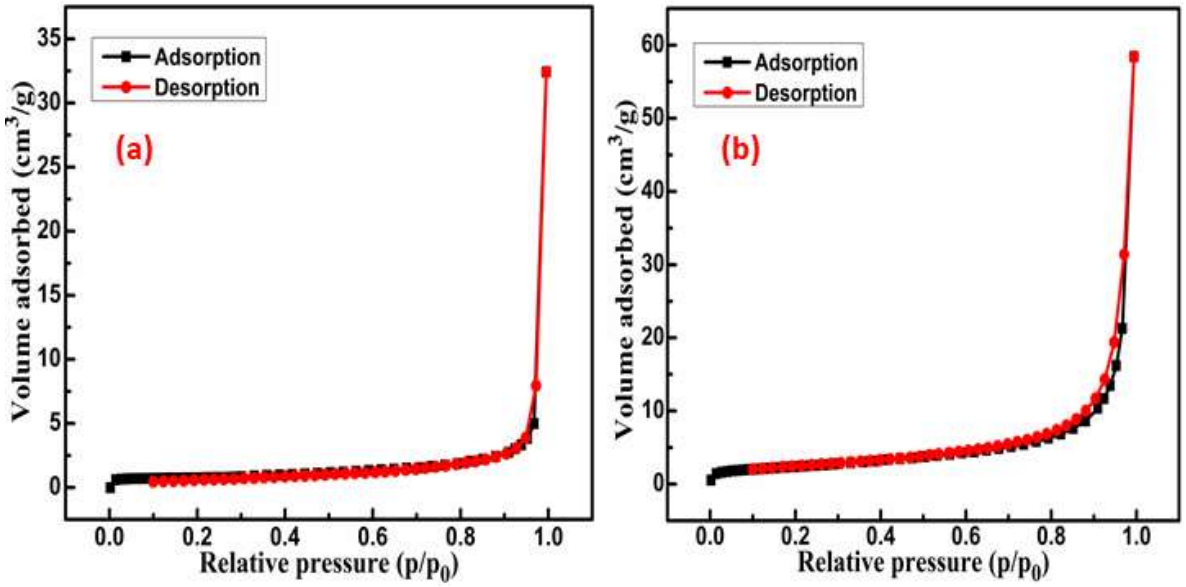

Fig. 5.6 N_2 adsorption-desorption isotherm for (a) A-1, and (b) AB-2

5.5 Optical bandgap analysis

The UV-DRS absorbance spectrum of the sample A-1 and B-1 is given in the figure 5.7a and b respectively; the absorption edges of the samples was found in the range of 250–300 nm. In order to illustrate the photocatalytic mechanism, the band gap energy of the materials was measured.from the UV-Vis DRS data by using equation (3.2).

Figure 5.7c and d displays the band gap of A-1 and B-1 respectively which, were obtained by plotting the graph between $(\alpha h\nu)^2$ and hv and extrapolating the intercept of the tangent on X-axis. The bandgap value for the sample A-1 and B-1 was found to be 3.16 and 3.10 eV respectively.

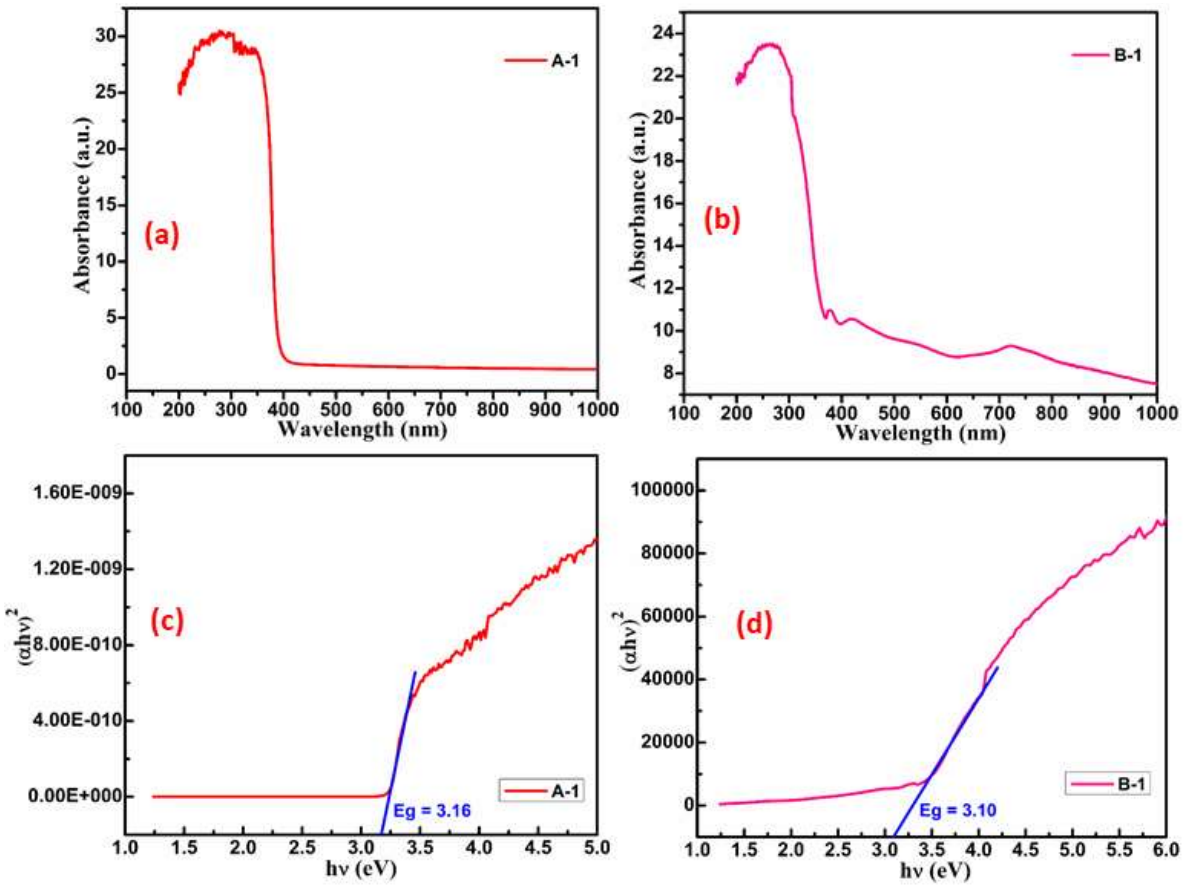

Fig. 5.7 UV-Vis DRS absorbance spectra of (a) A-1 (b) B-1 (c, d) Tauc plots of A-1 and B-1 respectively

5.5.1 Photoluminescence (PL) Study

Figure 5.8 displays the photoluminescence spectra of A-1, AB-1, AB-2 and AB-3 samples. The PL intensities of the NiS/ZnO nanocomposites (AB-1, AB-2 and AB-3) are found lower than that of pure ZnO nanoparticles. Moreover, the PL intensity of AB-2 is lowest among the nanocomposite samples. As we know that, the photoluminescence spectroscopy is related to study the transfer behavior of the photogenerated excitons and lower PL intensity indicates a restrained recombination of charge carriers (e^{-}/h^{+}) and consequently increased in photocatalytic performance (Mohamed Reda et al., 2017). Thus, the lowest peak intensity of AB-2 demonstrates the least recombination of photogenerated excitons and thus exhibits the better photocatalytic activity. It can be seen from the figure that after the optimum loading of NiS (AB-2) further increase in the loading of NiS will increases the PL intensity; which means that the excessive amount of NiS blocks the access of light to the surface of ZnO and in that case we get lower activity of the photocatalyst.

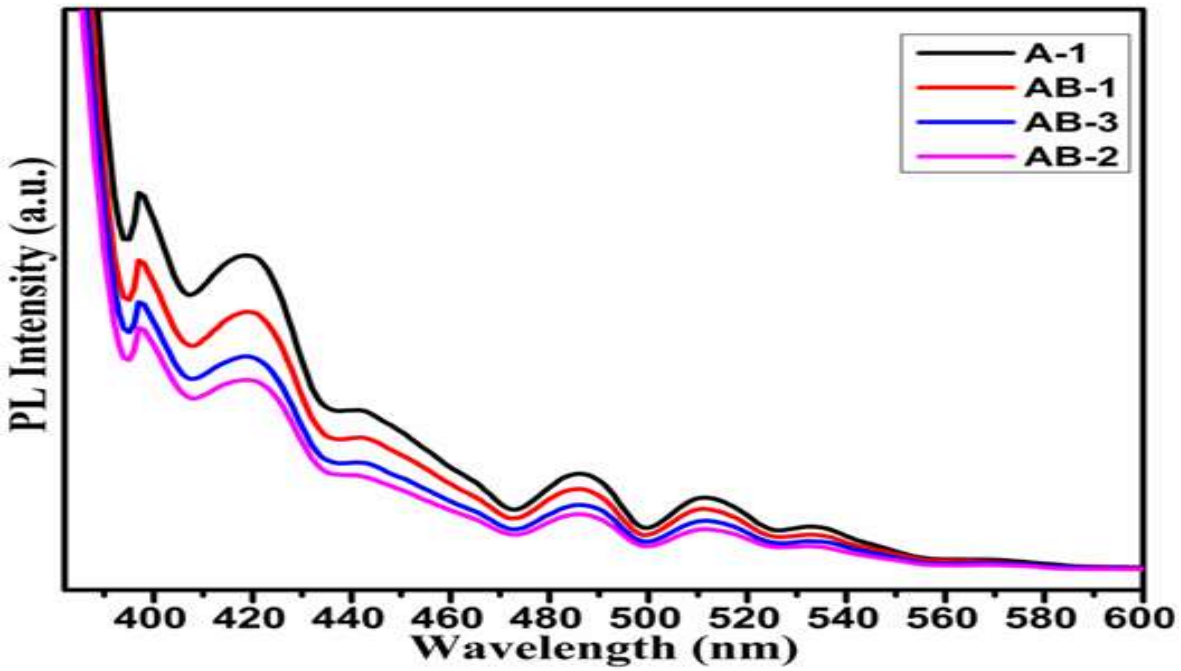

Fig. 5.8 PL spectra of A-1, AB-1, AB-2, and AB-3 samples

5.6 Evaluation of photocatalytic efficiency

In order to evaluate the photocatalytic performances of the prepared samples; photocatalytic degradation of the eminent organic pollutant p-nitrophenol (PNP) and RhB dye was investigated in aqueous solution under UV-light.

5.6.1 Photocatalytic degradation of PNP

The results of photocatalytic degradation of PNP are given in the figure 5.9; from figure 5.9a, it can clearly be seen that the characteristic peak of PNP undergoes red shift (from 315 nm to 399 nm) after the addition of photocatalyst (pH 8.5). The observed shift is due to conversion of PNP into p-nitrophenolate ion which is more active than PNP (Hernández-Gordillo et al., 2015,; Gómez-Solís et al., 2019). It was observed that the peak of p-nitrophenolate do not undergo any change in absorbance without the addition of photocatalysts. To determine the activity of the synthesized samples the disappearance of the characteristic absorption peak of p-nitrophenolate (399 nm) was monitored.

Figure 5.9b displays the variation in the absorbance spectra of p-nitrophenolate with time under UV-light irradiation over AB-2 photocatalysts, as can be seen from the figure, the peaks of p-nitrophenolate almost disappeared in 120 min. The degradation percentage of p-nitrophenolate by various synthesized samples is shown in figure 5.9c, which reveals that A-1 degrades 65% of p-nitrophenolate and B-1 degrades only 16%. However, nanocomposites (AB-1, AB-2 and AB-3) display higher degradation efficiency towards pollutant than pure A-1 and B-1 photocatalyst. Moreover, among all the synthesized nanocomposites AB-2 is the most efficient which degrades 96% of p-nitrophenolate ion from the aqueous suspension while AB-1 and AB-3 degrades 78% and 84% respectively. In the dark condition almost 5% of the p-nitrophenolate was adsorbed over the surface of AB-2.

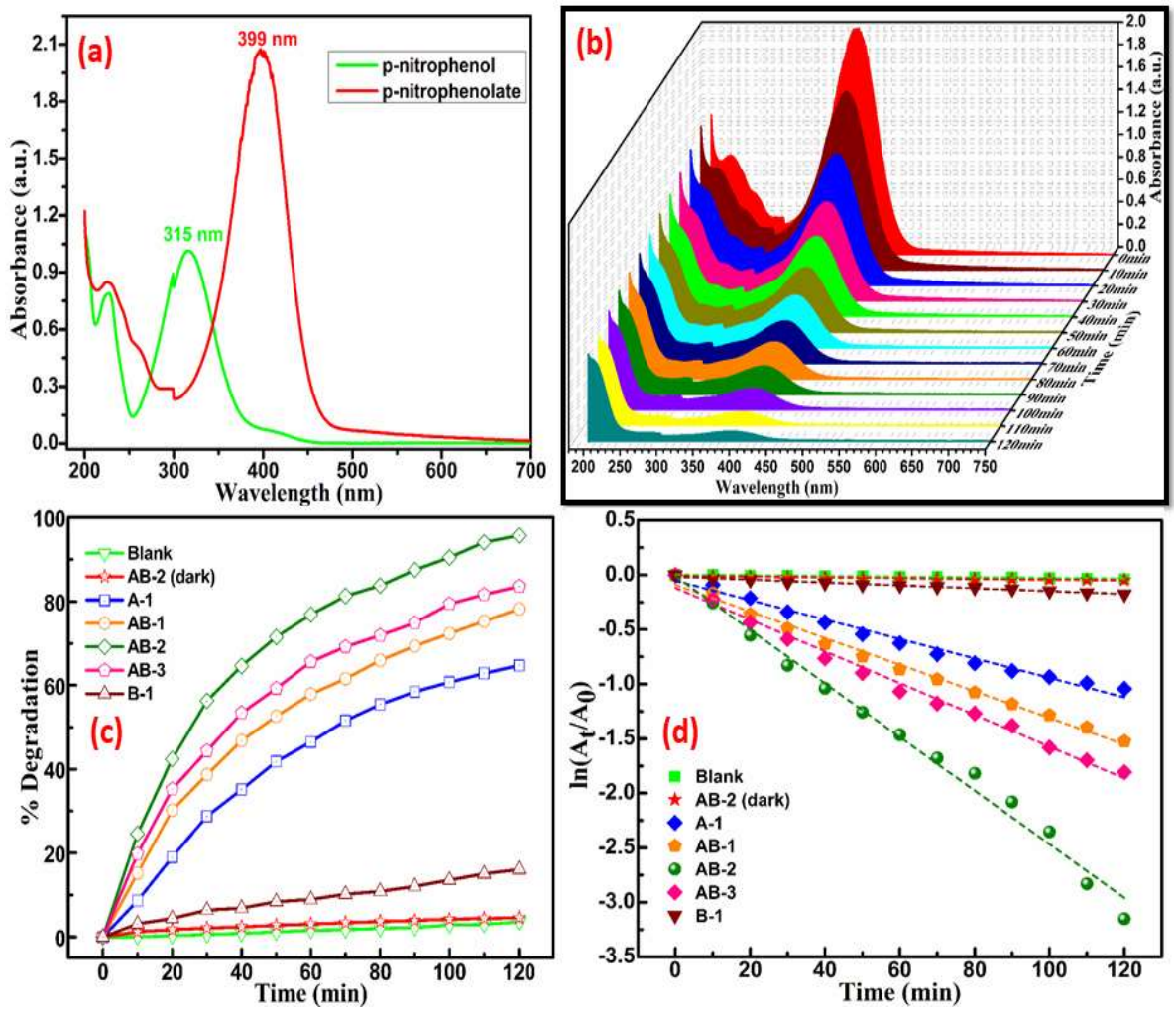

Fig. 5.9 (a) Comparative shifts observed in the peak of PNP, (b) UV-Vis. Absorbance spectra of PNP with AB-2, (c) Comparative degradation (%) plot of PNP by different photocatalyst, and (d) Kinetic plots of PNP degradation

The kinetics of photocatalytic degradation of PNP was determined by using following equation (Ma et al., 2011; Sun et al., 2009).

$$\ln\left(\frac{C_t}{C_0}\right) = -k_{app}t \qquad (5.2)$$

Where, k_{app} and t signifies the apparent rate constant and time (min) respectively. The rate constant was calculated from the slope obtained between $\ln\left(\frac{C_t}{C_0}\right)$ and t. Kinetic plot of PNP

degradation is given in figure 5.9d. The rate constant was calculated for all the samples and it was found that AB-2 have highest rate constant (2.46×10^{-2} min^{-1}) and the linear fitting of curve reveals that photocatalytic degradation follow pseudo 1st order mechanism.

5.6.2 Photocatalytic degradation of RhB

The efficiency of the as prepared photocatalysts was also evaluated by examining the change in the absorbance of RhB dye with time under UV-light illumination. Results of the photocatalytic experiment are given in the figure 5.10; the figure 5.10a shows the characteristic peak of RhB dye appeared at 554 nm. Hence, during the photocatalytic degradation we observed the continuous change in the absorbance of this peak (554 nm) as the time passes.

Figure 5.10b shows the UV-Vis absorbance spectra of RhB degraded over the AB-2 photocatalyst which depicts a sharp decrease in the absorbance of RhB with time; moreover, from the figure 5.10c we observed the degradation percentage of the above mentioned dye by different photocatalysts. It can be clearly seen from the figure that nanocomposite photocatalysts (AB-1, AB-2 and AB-3) remove higher percentage of the dye from the suspended solution than pure A-1 and B-1 photocatalyst. However, among all the synthesized photocatalyst AB-2 degrades highest percentage (93%) of the dye while, AB-1, AB-3, A-1 and B-1 removes only 80, 87, 68 and 18% of RhB dye. The kinetic plot of the photocatalytic degradation experiment is shown in the figure 5.10d from the slope of this plot rate constant was calculated by using the equation (5.2). The calculated rate constant was found to be highest for the AB-2 (2.50×10^{-2} min^{-1}) photocatalyst. The linear fitting of the slope indicates that in this case degradation also follows pseudo 1st order kinetics.

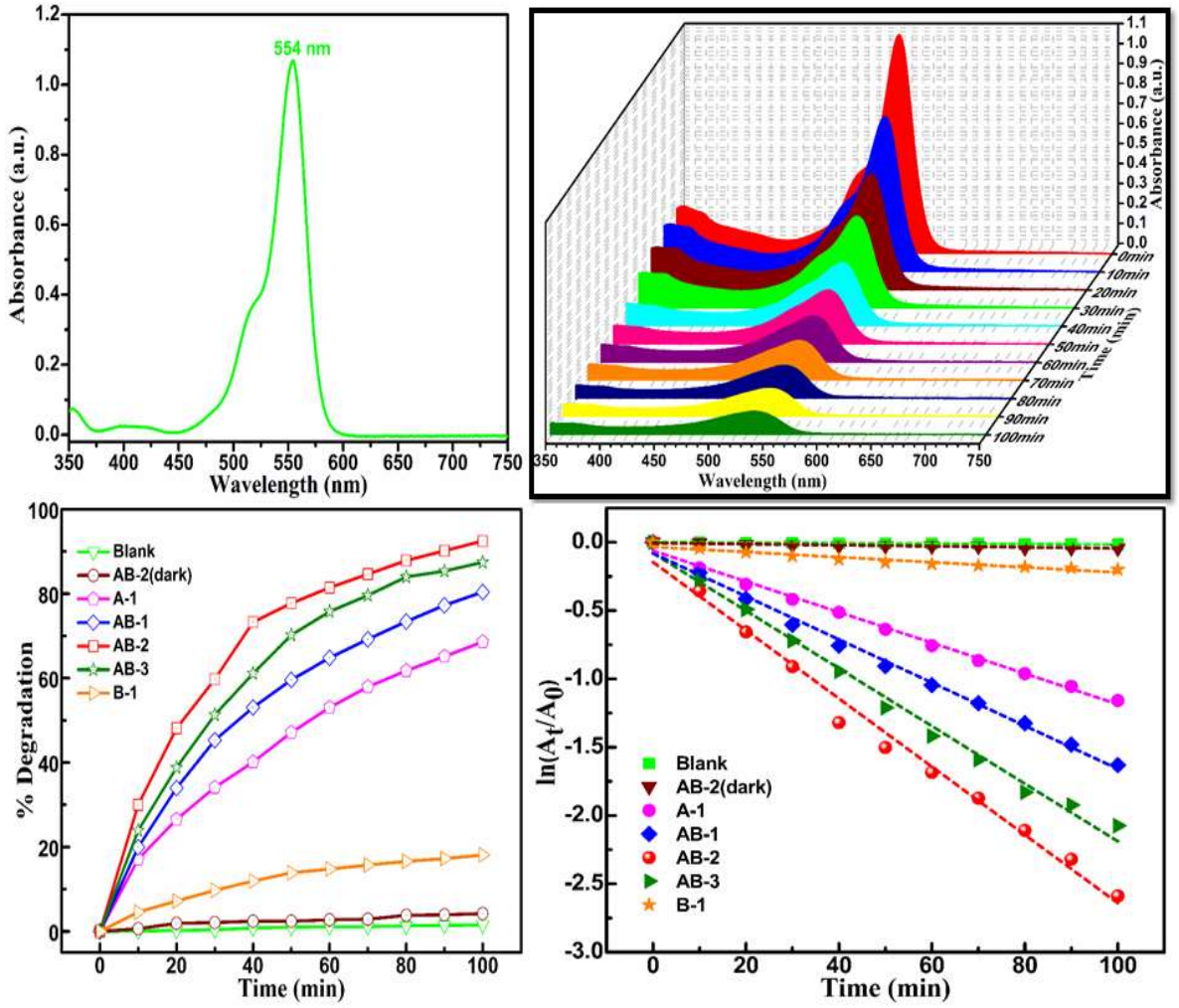

Fig. 5.10 (a) Showing characteristic UV-Vis absorbance peak of RhB, (b) UV-Vis absorbance spectra showing photocatalytic degradation of RhB by AB-2, (c) Percentage photocatalytic degradation of RhB by different photocatalyst, and (d) Kinetic plot for RhB degradation

5.6.3 Effect of NiS content

In order to know the effect of loading of NiS over ZnO nanoparticles a series of photocatalytic degradation experiment of PNP and RhB dye was carried out. The result of degradation experiment is given in figure 5.9c and figure 5.10c, which depict that nanocomposites (AB-1, AB-2 and AB-3) have higher photocatalytic degradation efficiency

than pure nanoparticle (A-1 and B-1). However, we observed that initially increasing the loading amount of NiS (from AB-1 to AB-2) the photocatalytic efficiency increased due to efficient charge separation between electrons and holes but after an optimum amount further loading of NiS (from AB-2 to AB-3) suppresses the efficiency of the photocatalyst; this happens because the increased amount of NiS covers the surface of ZnO and caused agglomeration of charges, moreover, due to screening of ZnO surface, the interfacial assembly between NiS and ZnO are braked and photocatalytic activity get reduce.

5.6.4 Scavenger experiments

Since during the process of photocatalytic degradation some reactive intermediates like anionic superoxide radicals ($O_2^{\bullet-}$), hydroxyl radicals ($OH^{\bullet}$), and holes (h^+) are formed by illumination with suitable light sources (Yu et al., 2012; Zhang et al., 2010). So in order to determine the most active species formed during the photocatalysis of AB-2 a series of trapping experiments was carried out separately with various scavengers such as KI (h^+ quencher), PBQ ($O_2^{\bullet-}$ radical trapper) and IPA ($OH^{\bullet}$ radical quencher) under UV-light.

The results of trapping experiment is given in figure 5.11 which depicts that when photocatalysts was used without adding scavenger it degrades almost 72% of PNP in 50 min, however when it was used with scavengers the degradation efficiency of the photocatalysts got suppressed. Moreover, the degradation of PNP is greatly suppressed after adding IPA while with PBQ and KI the degradation is slightly suppressed which indicates that hydroxyl ($OH^{\bullet}$) radical is the major reactive species generated during photocatalytic process alongwith superoxide ($O_2^{\bullet-}$) radical and holes (h^+). So, the order of reactive species generated during photocatalysis is as follow $OH^{\bullet} > O_2^{\bullet-} > h^+$.

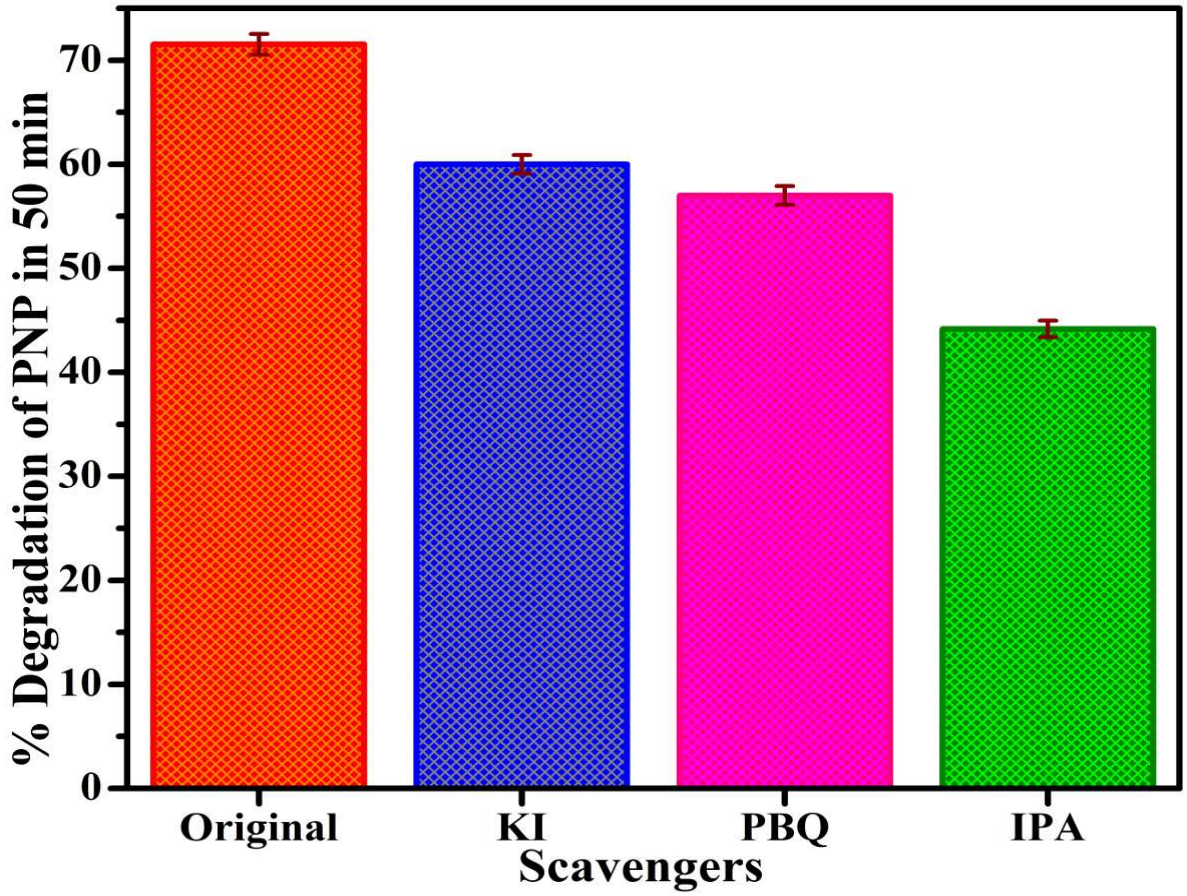

Fig. 5.11 Result of trapping experiment

5.7 Mechanism of photocatalytic reaction

The possible mechanism of the photocatalysis can be proposed from the band gap analysis as well as data obtained from trapping experiment. In fact, proper utilization of light energy and restrained rate of photo-generated charge recombination favor the process of photocatalysis (Pan et al., 2012). The absorption of UV-light by nanocomposite NiS/ZnO results in generation of excitons. It is known that nanocomposites having well-matched band position improves the e^{-}/h^{+} separation, resulting to which the photocatalytic activity gets increased (Yu et al., 2014). The position of the conduction band (CB) and valence band (VB) of NiS and ZnO were determined by using equations (3.4) and (3.5) respectively.

The estimated CB of ZnO and NiS were aligned at -0.29 and -0.82 eV respectively, however

the VB of the ZnO was positioned at 2.87 eV while VB of NiS was at 2.28 eV. The positions of the CB and VB of both the semiconductor possessed favorable band structure to separate the photogenerated charge carriers. Figure 5.12 displays the plausible mechanism for photocatalytic degradation of of PNP and RhB after irradiating AB-2 photocatalyst by UV-light source. When the photocatalyst was irradiated by UV-light the electron gets excited from the VB to the CB both the ZnO and NiS simultaneously. However, the photogenerated electrons and holes present in the CB of ZnO and VB of NiS respectively do not have sufficient reduction (CB = -0.29 eV) and oxidation (VB = 2.28 eV) potential to produce superoxide ($E_{O_2/O_2^{\bullet-}} = -0.33$ eV) and hydroxyl ($E_{OH^-/OH^{\bullet}} = 2.40$ eV) radical (Li et al., 2021; Zhang et al., 2019; Fu et al., 2015).

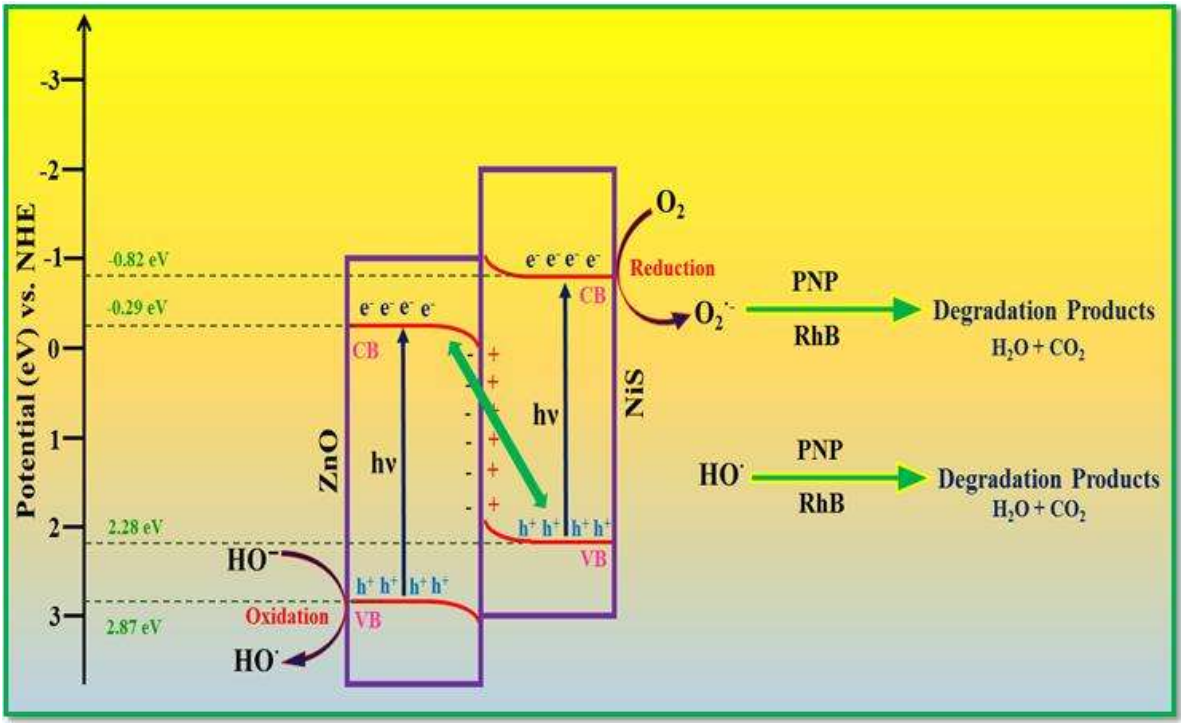

Fig. 5.12 Plausible mechanism of photocatalysis

Hence, they probably may be inactive and get recombined by the action of band bending interaction as well as internal electric field. Moreover, the electrons in the CB of NiS and

holes in the VB of ZnO remain intact and because of their well matched reduction and oxidation potential they ultimately produce $O_2^{\bullet-}$ and $OH^{\bullet}$ radical intermediate respectively to carry out the degradation of PNP and RhB dye. So, in brief the overall photocatalytic mechanism follows feasible and effective S-scheme (step scheme) pathway.

5.8 Turn over frequency (TOF)

As we know that TOF of catalysts determines their efficiency, i.e. higher the TOF more efficient is the catalyst (Pandey et al., 2021b; Zyoud et al., 2015). TOF value can be calculated with the help of equation (3.6).

The comparative results of the calculated TOF value of AB-2 photocatalyst alongwith the previous findings on PNP removal under UV irradiation is given in Table 5.1; which shows that our photocatalyst (AB-2) gives best result than previous articles cited in the table.

Table 5.1 Compare the TOF value of present investigation with previous study on photocatalytic removal of PNP

Sr. No.	photocatalyst	Light source	TOF (mole $g^{-1}min^{-1}$)	Reference
1.	Eu_2O_3/Ta_2O_5	Mercury lamp (50W, 313nm)	5.43×10^{-7}	(Yang et al., 2008)
2.	GO/ZnO	UV light source	9.50×10^{-7}	(Kale and Thakur, 2015)
3	Ag/ZnO	UV light source	3.99×10^{-6}	(Divband et al., 2013)
4.	MSnO3 (Ca, Ba, Sr)	UV lamp (254 nm)	2.65×10^{-6}	(Gómez-Solís

				et al., 2019)
5.	Ir/CeO2	Mercury lamp (UV lamp, 254nm)	1.01×10^{-6}	(Castañeda et al., 2019)
6.	***NiS/ZnO (AB-2)***	***UV-light (Phillips, 8 W, 254 nm)***	***6.73×10⁻⁶***	***This work***

5.9 Recyclability experiment

To examine the reusability and stability of the most efficient AB-2 nanocomposite, the photocatalytic degradation experiment of PNP with used AB-2 was repeated till 4th cycle.

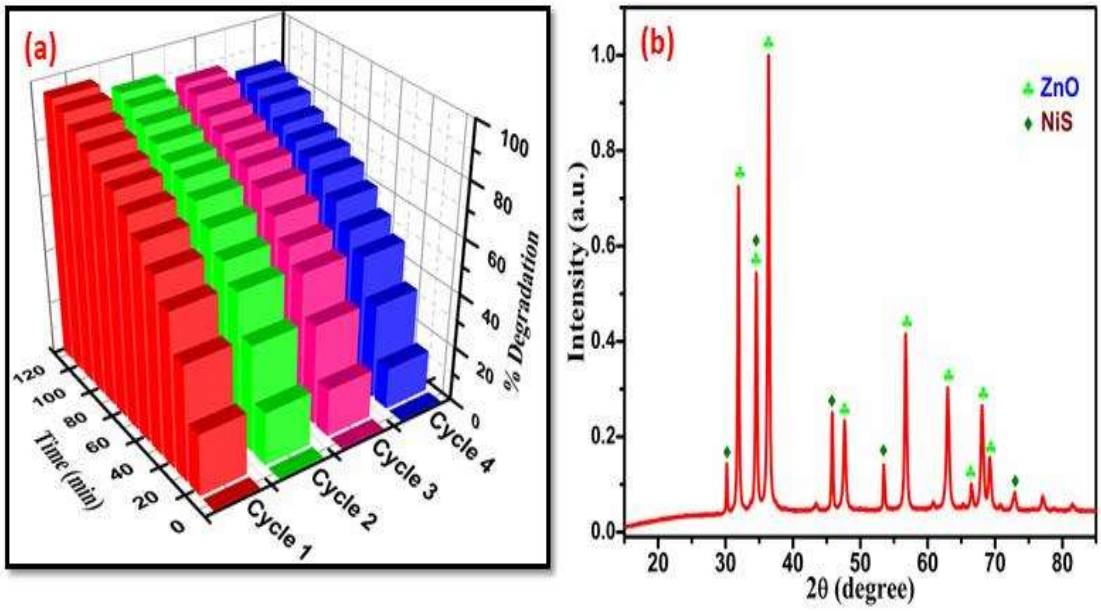

Fig. 5.13 (a) Recyclability test of AB-2 by photocatalytic degradation of PNP (b) HR-XRD pattern of reused AB-2 photocatalysts

The result of recyclability test is displayed in the figure 5.13a which indicates that nearly 11% decrement is observed even after 4th cycle.

The stability of the photocatalysts (AB-2) was also checked by characterizing reused samples

through HR-XRD and the result is shown in figure 5.13b which reveals that no phase change was observed and all the peaks are well matched with the original nanocomposite photocatalyst (AB-2) which supports the stability of the most efficient photocatalysts.

5.10 Summary and conclusions

On the basis of above results and discussion, we conclude that NiS/ZnO nanocomposites were synthesized by hydrothermal method. The synthesized AB-2 nanocomposite is spherical in shape and its average particle size is of 34 nm. The nanocomposite provides larger surface area than pure ZnO (A-1) for photocatalysis. The activity of the prepared samples was monitored by the photocatalytic degradation of PNP and RhB under the exposure of UV-light; it was found that AB-2 displays optimum PL as well as highest photocatalytic efficiency among all the synthesized samples. The rate constant for the degradation of PNP and RhB by AB-2 is 2.41×10^{-2} and 2.50×10^{-2} min^{-1} respectively. In the process of photocatalysis we achieve the appreciable TOF value which is highest among the TOF of citing literature in Table 5.1. The highest photocatalysis shown by AB-2 nanocomposite is mainly due to restrained charge recombination and strong redox potential of the useful electron and holes, hydroxyl ($OH^{\bullet}$) radicals are the primary reactive species generated during the process of photocatalysis along with h^{+} and $O_2^{\bullet-}$ radical.